Chemosphere 239 (2020) 124745

Contents lists available at ScienceDirect

Chemosphere

journal homepage: www.elsevier.com/locate/chemosphere

A facile foaming-polymerization strategy to prepare 3D MnO_2 modified biochar-based porous hydrogels for efficient removal of Cd(II) and Pb(II)

Zhiying Wu [a, b], Xiaoxiao Chen [a, **], Baoling Yuan [c], Ming-Lai Fu [a, *]

[a] Key Laboratory of Urban Pollutant Conversion, Institute of Urban Environment, Chinese Academy of Sciences, Xiamen, 361021, China
[b] University of Chinese Academy of Sciences, Beijing, 100039, China
[c] College of Civil Engineering Huaqiao University, Xiamen, 361020, China

HIGHLIGHTS

- A 3D MnO_2 modified biochar-based porous polyacrylamide gel (MBCG) was fabricated.
- The incorporated MBC endows MBCG with enhanced physicochemical properties.
- The porous structure equips MBCG with effective removal of Cd(II) and Pb(II).
- The spent MBCG can be easily separated and shows an excellent reusability.

GRAPHICAL ABSTRACT

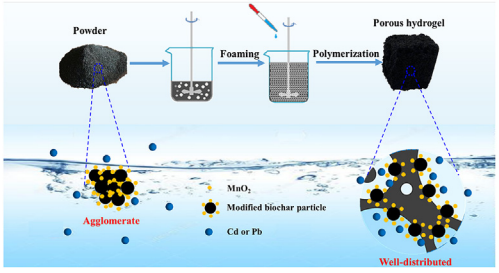

ARTICLE INFO

Article history:
Received 14 July 2019
Received in revised form
30 August 2019
Accepted 2 September 2019
Available online 3 September 2019

Handling Editor: Y Yeomin Yoon

Keywords:
Modified biochar
Polyacrylamide gel
Adsorbent
Heavy metal
Easy separation

ABSTRACT

A novel three dimensional MnO_2 modified biochar-based porous hydrogel (MBCG) was fabricated to overcome the low sorption capacity and difficulty in solid-liquid separation of biochar (BC) for Cd(II) and Pb(II) removal. BC was initially modified by a rapid redox reaction between $KMnO_4$ and Mn(II) acetate, and then incorporated into a polyacrylamide gel network via a rapid and facile free-radical polymerization. A foaming method was deliberately introduced during the fabrication to establish interpenetrated porous structure inside the network. Various characterizations were employed to examine the morphology, porous structures, chemical compositions, and mechanical properties of the samples. Adsorption performance of MBCG on Cd(II) and Pb(II) (isotherms and kinetics) as well as its desorption and reusability were also investigated. The results indicated that MnO_2 modified biochars (MBC) were successfully introduced and homogeneously distributed in the porous bulk hydrogel, endowing MBCG with more uniform pore structure, excellent thermostability, remarkable mechanic strength, and superior adsorption performance. The maximum Langmuir adsorption capacity on Cd(II) and Pb(II) is 84.76 and 70.90 mg g^{-1}, respectively, which is comparable or even larger than that of MBC. More importantly, MBCG can be rapidly separated and easily regenerated with an excellent reusability, which could retain 92.1% and 80.5% of the initial adsorption capacities of Cd(II) and Pb(II) after five cycles. These new insights make MBCG an ideal candidate in practical applications in water treatment and soil remediation contaminated with various heavy metals.

* Corresponding author.
** Corresponding author.
E-mail addresses: xxchen@iue.ac.cn (X. Chen), mlfu@iue.ac.cn (M.-L. Fu).

https://doi.org/10.1016/j.chemosphere.2019.124745
0045-6535/

1. Introduction

Heavy metals as one kind of specific contaminants in ecosphere have been greatly concerned due to their extreme toxicity, resistant biodegradable and long-term adverse effects on human health and natural ecosystems (Fu and Wang, 2011). Among them, cadmium (Cd) and lead (Pb) have long been identified as the most major human health hazards since Cd can cause serious damage to both kidneys and bones, while Pb is poisonous to the central nervous system and genital system (Mohan et al., 2014; Godiya et al., 2019). Therefore, a variety of remediation techniques have been developed to remove Cd and Pb, including chemical precipitation (Matlock et al., 2002), ion exchange (Vaca Mier et al., 2001), biological degradation (Chipasa, 2003), membrane filtration (Getachew et al., 2016), adsorption (Zhang et al., 2013b), *etc*. Adsorption is considered as one of the most practical approaches for the removal of heavy metals due to its flexible design, simple operation, high effectiveness and availability of different adsorbents.

During the past decades, various sorbents has been widely studied to remove Cd and Pb from contaminated water, such as activated carbon (Lo et al., 2012), lignin (Demirbas, 2004), zeolite (Wingenfelder et al., 2005), biosorbents (Wang and Chen, 2014), and metal organic frameworks (Burtch et al., 2014). Biochar obtained from the thermal decomposition of biomass under oxygen-limited conditions has caught increasing attention for its highly-porous structure, large surface area, and various oxygen functional groups (e.g., carboxyl, hydroxyl, and phenolic groups) (Chen et al., 2012; Li et al., 2017). Recently, numerous studies have studied the application of biochar produced from various feedstocks (wood bark, dairy manure, sugar beet tailing, pinewood, and rice husk) under different pyrolysis conditions (temperature, heating transfer rate, and residence time) in the removal of various heavy metals, such as arsenic (As), Cd, chromium (Cr), mercury (Hg), and Pb (Oliveira et al., 2017; Xiao et al., 2018). However, the limited adsorption capacity of bare biochar and the difficult recovery of the spent powder-type biochar make it hard to be implemented in the real application.

Incorporation of inorganic nanoparticles into biochar is considered as an effective approach to enhancing its adsorption performance (Rajapaksha et al., 2016). As one of the typical examples, manganese oxide (MnO_2) has attracted great interests due to its high surface area, strong surface reactivity, and prevalent existence in terrestrial environments (Wang et al., 2018). More importantly, the point of zero charge (pH_{pzc}) of MnO_2 is 2–3 (Morgan and Stumm, 1964), which makes it negatively charged near neutral pH and thus could effectively capture positive species due to the electrostatic attraction. Liang et al. synthesized MnO_2 modified biochars through a rapid redox reaction between $KMnO_4$ and Mn(II) acetate solution, which showed an obvious enhanced capacity of Cd(II) and Pb(II) sorption compared to the pristine biochar (Liang et al., 2017). Wang et al. found that hydrous manganese oxide modification of peeled pine wood biochars exhibited 4-fold higher Pb(II) sorption capacity than parent BCs (Wang et al., 2015b). Based on these observations, loading MnO_2 nanoparticles onto the biochar can be an effective approach to enhancing the adsorption capacity of raw biochar. On the other hand, to solve the difficult separation of biochar, assembling biochar into three dimensional (3D) architectures has been recognized as a more promising method than modifying biochar with magnetic particles as it can be easily removed without any external magnetic field (Zhang et al., 2013a; Liu et al., 2016). Strikingly, polyacrylamide gel (PAMG) has been widely used as the supporting matrix for various nanoparticles because of its 3D network structure which just makes up for the limitation of separation and regeneration on the particulate adsorbents. Besides, its excellent properties such as biocompatibility, biodegradability and easily available in natural resources, further make it an ideal material for potential heavy metal adsorption (Dong et al., 2018).

The objective of this study is to design a new multifunctional material based on the synthetic properties of MnO_2 loaded biochars and 3D PAMG to overcome the low sorption capacity and difficulty in solid-liquid separation of BC. Herein, BC was initially modified via a rapid redox reaction between $KMnO_4$ and Mn(II) acetate solution, followed by an incorporation into the PAMG network through a rapid and facile free-radical polymerization. Furthermore, a pore foaming process was deliberately introduced during the fabrication to establish interpenetrated porous structure inside the bulk material. The physicochemical properties of the as-synthesized adsorbents were extensively characterized by SEM-EDX, TEM, XPS, FT-IR, BET, TGA, etc. The adsorption performances for Cd(II) and Pb(II) (kinetics and isotherms) as well as desorption and regeneration abilities were also explored. As for comparisons, unmodified biochar, modified biochar, blank gel (i.e., pure PAMG), and unmodified biochar gel were also prepared as controls. This study can offer new insights into the trapping of Cd(II) and Pb(II) and broaden the practical applications of such biochar-based composites in environmental pollution control, which would not cause secondary pollution.

2. Experimental

2.1. Materials

All chemicals in this study except acrylamide (industrial reagent grade) were of analytical reagent grade and used without further purification. Manganese acetate tetrahydrate ($Mn(CH_3COO)_2{\cdot}4H_2O$), potassium permanganate ($KMnO_4$), sodium dodecyl sulfate ($C_{12}H_{25}NaO_4S$), N, N, N′, N′- tetramethylethylenediamine (TMEDA), sodium persulfate ($Na_2S_2O_8$), lead nitrate ($Pb(NO_3)_2$), cadmium nitrate tetrahydrate ($Cd(NO_3)_2{\cdot}4H_2O$), and sodium nitrate ($NaNO_3$) were obtained from Sinopharm Chemical Reagent Co., Ltd (China). N, N′-methylenebisacylamide (MBA) was purchased from Aldrich-Sigma (China). Acrylamide (AM) was purchased from Jiangxi Changjiu Nongke Chemical Co., Ltd (China). Rice husks were used as the feedstock of biochar, which were obtained from an agricultural field in Anhui Province, China. Stock solutions (1000 mg L^{-1}) of Cd(II) and Pb(II) were prepared by dissolving exact quantities of the respective salts in the background solution containing 0.01 M $NaNO_3$. The relevant working solutions used in the batch experiments were obtained through proper dilution of these stock solutions before testing and the pH values were adjusted by adding 0.01 M HNO_3 or NaOH solutions (The pH of Cd(II) solution was 6.0 ± 0.05 and the pH of Pb (II) solution was 4.0 ± 0.05).

2.2. Preparation of biochar (BC) and MnO_2 modified biochar (MBC)

To prepare the biochar (BC), the rice husks were first washed with deionized water for three times, then dried at 80 °C for 24 h and further milled to pass through a 0.154 mm sieve. The powdered biomass was then tightly packed into a ceramic pot (300 mL), covered with a fitting lid, and pyrolyzed at 500 °C in a muffle furnace for 2 h. The heating speed was controlled at 5 °C min^{-1} for a slow pyrolysis to produce more solid residue (biochar) (Chen et al., 2012).

The MnO_2 modified biochar (MBC) was synthesized following the method described by Liang et al. (2017): 15 g of BC and 3.16 g of $KMnO_4$ were mixed in 150 mL of deionized water(DI) with vigorous

stirring at room temperature, and then the suspension was ultrasonically oscillated for 0.5 h to ensure the full contact of BC and $KMnO_4$. After that, 100 mL of Mn(II) acetate tetrahydrate solution (0.3 M) was added dropwise under continuous stirring, producing dark brown precipitation of MnO_2 in the suspension according to Eq. (1).

$$3Mn^{2+} + 2MnO_4^- + 2H_2O = 5MnO_2 + 4H^+ \quad (1)$$

Following that, the resulting suspension was heated to 80 °C and kept at this temperature for an additional 30 min to get the MBC suspension before filtration. Finally, BC and MBC were washed with DI water several times and oven-dried at 80 °C, respectively, and then they were ball-milled to pass through a 100 mesh sieve and preserved in the desiccator prior to use.

2.3. Synthesis of the modified biochar gel (MBCG)

The modified biochar hydrogels (MBCG) were prepared via a free-radical polymerization method by the following procedures. Initially, 3.6 g of AM, 0.3 g of MBA (as a cross-linker), 15 g of MBC, and 20 mL of DI water were mixed in a mill pot, then the mixture was ball milled for 60 min to transform the solid-liquid amalgam to the homogeneous slurry. Following that, the resulting slurry was transferred into a beaker and then 0.03 g of sodium dodecyl sulfate was added into the homogeneous slurry with vigorously mechanical stirring for 20 min to foam the slurry until it expands to a designed volume. Thereafter, 1.2 mL of TMEDA (as a catalyst) was introduced under the vigorously mechanical stirring for 5 min, followed by addition of 5 mL of $Na_2S_2O_8$ solution (10 wt%) into the foaming slurry to trigger the crosslinking reaction. The resulting foaming slurry was then transferred to a row of cubic molds where the solid hydrogels were formed after a few minutes. Finally, the as-prepared hydrogels were rinsed, freeze-dried and stored for further use. For comparisons, neat BC hydrogel (BCG) and pure PAM hydrogel (BG) were prepared according to the same procedure, respectively.

2.4. Characterizations

The microstructures of the samples were characterized by a Hitachi S-4800 emission scanning electron microscope equipped with an energy dispersive X-ray (EDX) system and the crystalline lattice parameter was investigated by the TEM (Tecnai G2 F20, USA). The valances of specific elements were analyzed by energy dispersive X-ray spectroscopy (XPS, K-Alpha, Thermo Fisher Scientific, England), and all the binding energies were calibrated using C 1s peak (284.8 eV). A curve-fitting program (XPS-peak 4.1 software) was used to fit the XPS results under Shirley background. The crystallite phase composition was analyzed using powder X-ray diffraction (XRD), which was performed by an X'Pert PRO diffractor (PANalytical, Holland, Cu $K_{\alpha,\ \lambda} = 0.15406$ nm) with the tube parameters (40 kV of voltage and 40 mA of current). FT-IR spectra were provided by a Thermo Scientific Nicolet spectrophotometer (iS10) using pellets with KBr powder. The specific surface area and pore distribution of the samples were analyzed by N_2 adsorption-desorption at the liquid N_2 temperature (−196 °C) using an ASAP-2020 M analyzer (Micrometrics Inc., USA). Before measurement, samples were degassed under vacuum (to less than 0.1 Pa) at 100 °C for 12 h. The specific surface area was calculated by the BET (Brunauer-Emmett-Teller) method using adsorption data. The pore radius distribution was obtained from the adsorption branch by the BJH (Barret-Joyner-Halenda) method. The thermal gravimetric analysis (TGA) (Netzsch TG 209 F3) was conducted to analyze the crystalline phase transformation temperature from 40 °C to 1000 °C at a rate of 10 °C min^{-1} under nitrogen atmosphere. The compressive tests of the gels were carried out by using a home-made universal testing machine (ZL-8001, China) fitted with a 50 N load cell. The compressive stress-strain response was measured at a strain rate of 0.05 mm s^{-1}. Three repeat measurements were tested for each sample in all the characterizations.

2.5. Batch adsorption experiments

Batch adsorption experiments were conducted by the traditional bottle-point method to explore the Cd(II) and Pb(II) sorption performance of as-prepared adsorbents. All the experiments were performed in 20 mL glass vials with each containing 20 mL solution. The dosages of BC, MBC, BCG, and MBCG used in Cd(II) adsorption experiments were set as 1, 0.3, 1, and 0.3 g L^{-1}, respectively, and the dosage of them in Pb(II) adsorption experiments were 0.5, 0.15, 1, and 0.3 g L^{-1}, respectively. All solution samples were shaken in an incubator shaker (ZHWY-2102C, ZhiCheng, Shanghai, China) with the desired temperature of 25 °C and fixed rotate speed of 200 rpm during the sorption process.

The adsorption kinetic experiments of Cd(II) and Pb(II) on BC, MBC, BCG, and MBCG were all performed at an initial concentration of 20 mg L^{-1} and then shaken for 72 h in the incubator shaker. At predetermined time intervals, replicate vials were sacrificially sampled to measure the surplus concentration of Cd(II) and Pb(II) in the liquid phase. The pseudo-first-order model and the pseudo-second-order model were employed to fit kinetic data for further analysis.

The adsorption isotherm experiments of Cd(II) and Pb(II) on BC, MBC, BCG, and MBCG were all established with concentrations ranging from 2 to 50 mg L^{-1} after a 24 h oscillation (as suggested from the preliminary kinetic study). Controls of heavy metal solutions without samples and controls of background solutions with samples were also carried out. The Langmuir and Freundlich models were employed to fit isotherm data for further analysis.

The regeneration and reuse studies of BCG and MBCG on Cd(II) and Pb(II) were carried out for five consecutive adsorption-desorption cycles. In each cycle, given amount of BCG was added into 100 mL of 50 mg L^{-1} Cd(II) and Pb(II) solution, respectively. While given amount of MBCG was added into 150 mL of 50 mg L^{-1} Cd(II) and Pb(II) solution, respectively. After 20 h of vibration, the spent gels were eluted with 0.3 M HNO_3 solution and regenerated with 0.03 M NaOH, further washed with deionized water until neutral condition. The next cycle of adsorption was carried out after freeze-dried. Changes in sorption capacity were determined at every cycle.

The initial and final residual concentrations of Cd(II) and Pb(II) in all the tests were analyzed by an Inductively Coupled Plasma Optical Emission Spectrometer (ICP-OES, 7000DV, Optima, USA) after the samples were taken and filtered through 0.22 μm filters. All tests were performed in duplicate for data analysis, and additional analyses were conducted whenever two measurements showed a difference of more than 5%. The removal efficiency (E%) and the amount of heavy metal ion absorbed (Qe, mg g^{-1}) were calculated using Eqs. (2) and (3), respectively.

$$E\% = \frac{(C_0 - C_e)}{C_0} \times 100\% \quad (2)$$

$$Q_e = \frac{(C_0 - C_e) \times V}{m} \quad (3)$$

where Q_e (mg g^{-1}) is the amount of heavy metal ion adsorbed per unit mass of the sorbent, C_0 and C_e (mg L^{-1}) are the initial and equilibrium liquid phase ion concentration, respectively, V (L) is the

volume of the solution and m (g) is the mass of the adsorbent.

3. Results and discussion

3.1. Preparation and characterization of adsorbents

The MBCG was synthesized according to the procedures as illustrated in Fig. 1. The BC was initially modified through a rapid redox reaction between $KMnO_4$ and Mn(II) acetate, and then the MBC were embedded in the PAMG by using a rapid and facile free-radical polymerization. A pore foaming process was deliberately introduced during the fabrication to establish interpenetrated porous structure inside the bulk material as indicated by the apparent volume expansion of slurry. After polymerization, the spongy hydrogel was formed and it could be easily cut into monolithic cubic bulks without structural cracks. Upon freeze-drying, the as-prepared hydrogels were dehydrated to black, light-weight, and porous aerogel bulks without any obvious shrinkages.

In order to verify the successful MnO_2 modification on biochars, SEM-EDX analysis was firstly conducted to investigate their morphological structure and surface elemental composition. Compared with the smooth surface of BC (Fig. S1), the surface of MBC was evenly covered with small particles. Similar phenomenon was also observed in other literatures related to MnO_2 modified biochars (Song et al., 2014; Liang et al., 2017). The corresponding EDX analysis shows the changes of elementary composition percentages (a slight increase of O and decrease of C) on MBC with the occurrence of new well-distributed elemental Mn. The TEM images (Fig. S2) corresponded with the morphology as presented in the SEM images. The surface of MBC was uniformly dispersed with irregular nanoparticles and the HRTEM image demonstrates lattice fringes with interplanar spacing of 0.221 nm, corresponding to the (2 0 0) plane of MnO_2, confirming the successful load of MnO_2 nanoparticles.

XPS analysis was further performed to investigate their chemical state and surface composition. The survey spectra indicate that no obvious impurities present in BC and MBC (Lai et al., 2019). As shown from the full-range XPS spectrum (Fig. 2a), two remarkable peaks (C 1s, O 1s) are both displayed in the pattern of BC and MBC while one new peak (Mn 2p) apparently appeared in that of MBC. By the elemental analysis, the C/O ratio of BC and MBC was 2.47 and 1.97, indicating that a small quantity of O-containing functional groups was introduced onto the biochar surface after modification, in accordance with the above EDX analysis. As shown in Fig. 2b and c, high resolution spectrum of C 1s spectrum of BC can be divided into four peaks, which could be assigned to sp^2 (C=C, 284.61 eV), sp^3 (C-C, 285.36 eV), bonded carbon (C-O, 286.25 eV), and carbonyl groups (C=O, 288.68 eV), respectively (Yang et al., 2018; Zhang et al., 2019a). A similar result was obtained for the deconvolution of C 1s spectrum of MBC, which indexed that these C-containing functional groups might not have a remarkable effect on the modification. Expanded spectra of element Mn 2p (Fig. 2d) displayed double peaks (Mn $2p_{3/2}$ and Mn $2p_{1/2}$) at the binding energy values of 642.2 and 653.8 eV. The spin-energy separation of 11.6 eV indicated that the predominant Mn oxidation state in synthesized MBR was Mn^{4+} (Liu et al., 2016), which is in accordance with the above TEM results.

To probe the effect of modification on the functional groups of BC, FTIR analysis was conducted and the resulting spectra are shown in Fig. 2e. For the spectrum of BC, the broad band around 3438 cm^{-1} and peak at 1383 cm^{-1} are associated with ν(-OH) vibration in hydroxyl groups (Xing et al., 2008; Song et al., 2014). The peaks at 1701 cm^{-1} and 1438 cm^{-1} are the characteristic peaks indicating C=O for carboxyl or traces of aldehydes, ketones, and esters. The peak at 1604 cm^{-1} referred to C=C in the aromatic ring. The most prominent peak at 1102 cm^{-1} can be assigned to the O-containing function groups of cellulose and hemicelluloses as well as the asymmetric stretching vibration of Si-O-Si (Zhu et al., 2019), which is consistent with the abundant Si content observed in the aforementioned EDX analysis. The peaks at 804 cm^{-1} and 468 cm^{-1} can be defined as the aromatic C-H banding and Si-O-Si vibration (Ahmed et al., 2016). After the impregnation of MnO_2, a new peak occurred at 570 cm^{-1} which accorded with Mn-O stretching vibration (Wang et al., 2018), also indicating that the surface of MBC has been successfully covered by MnO_2. Notably, the bands of hydroxyl groups and carboxyl groups were significantly shifted from 3438, 1701, and 1438 cm^{-1} to 3422, 1686, and 1420 cm^{-1}, revealing that MnO_2 is bounded on the surface of BC through interactions with these surface hydroxyl and carboxyl groups (Zhang et al., 2019b).

FT-IR measurements were also used to validate the successful polymerization of biochars with the results shown in Fig. 2f. The main signals in the BG exhibit the characteristic absorption peaks of polyacrylamide, including the peaks at 1655 cm^{-1} (C=O group of amide (amide I), 1616 cm^{-1} (deformation vibration of $-NH_2$ groups (amide II)), 1450 cm^{-1} ($-CH_2$), 1413 cm^{-1} and 1189 cm^{-1} (deformation vibration of −NH groups), 1316 cm^{-1} (stretching vibration of −NH groups) and 1116 cm^{-1} (C-N and N-H bonds (amide III)) (Kaşgöz et al., 2003). After incorporation of BC and MBC, the above

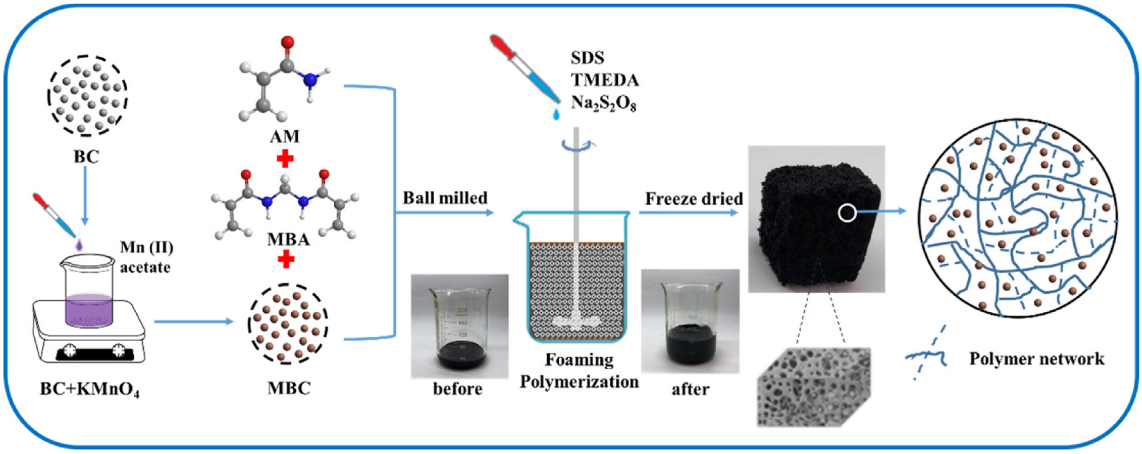

Fig. 1. Schematic illustration of the preparation process of MBCG.

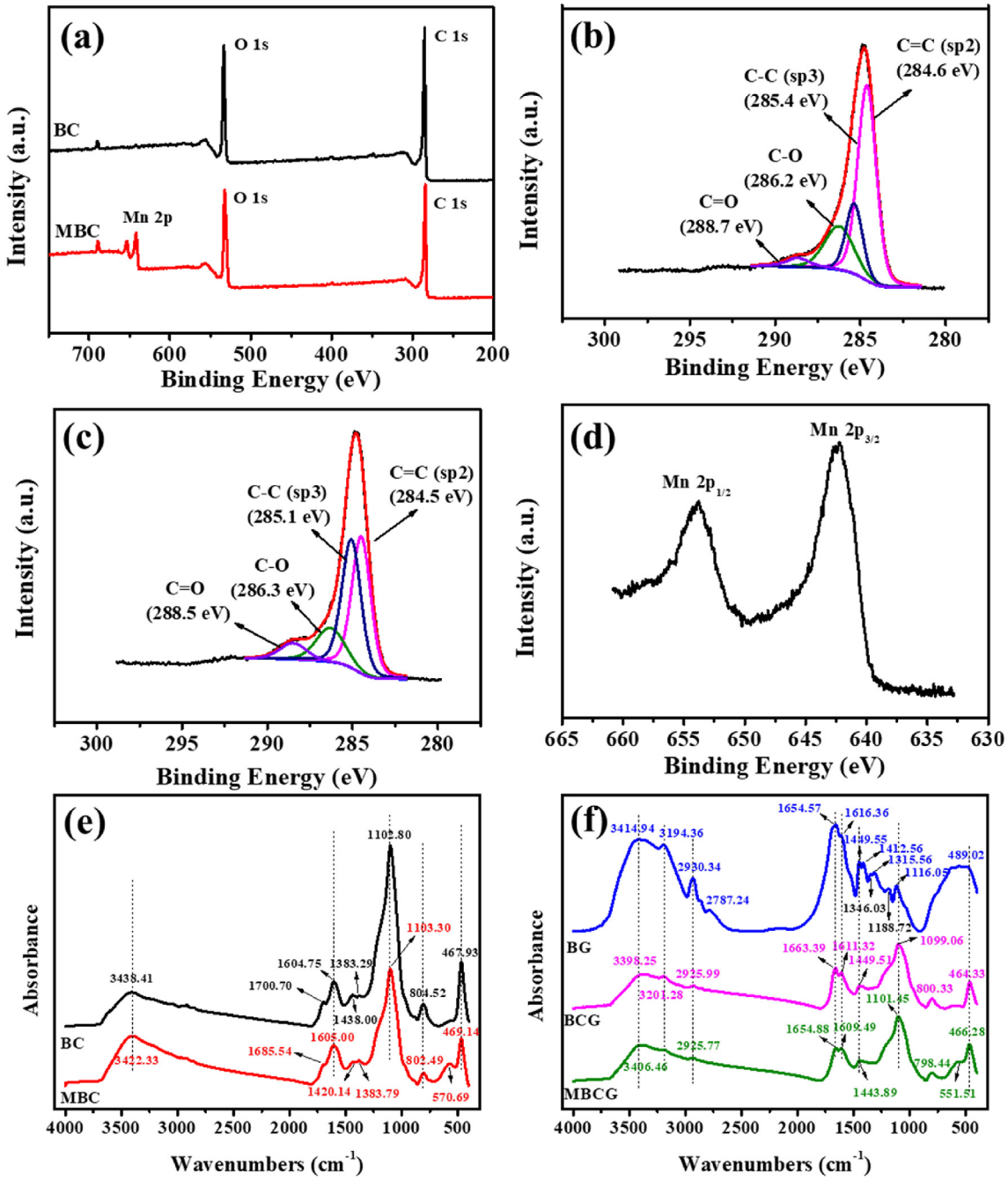

Fig. 2. XPS scan spectra of BC and MBC: (a) wide scan, (b) the deconvolution of C 1s spectrum for BC, (c) the deconvolution of C 1s spectrum for MBC, (d) Mn 2p; FTIR spectra (e, f) of BC, MBC, BG, BCG, and MBCG.

characteristic peaks shift to lower wavenumbers and some even disappeared in the spectra of BCG and MBCG. This phenomenon may be attributed to the presence of the hydrogen bonding interactions between the N–H bond of PAMG and O–H bond of biochars (Fan et al., 2013). Likewise, the new peak appeared at 551 cm^{-1} representing Mn-O stretching vibration also confirms the successful introduction of MnO_2. Taken together, the above-mentioned results evidenced that modified biochar composite gel was successfully synthesized.

The SEM images of the gels at two different magnifications are shown in Fig. 3, the insets are the corresponding digital photographs. As seen, the use of the pore-forming agent under vigorously mechanical stirring led to the formation of porous structures in all the gels. Specifically, the color of BG was white and its structure is uneven for the most part of it is porous and a small part is compact. After the introduction of BC and MBC, the characteristics of BCG and MBCG are quite different from BG as both of them exhibit black and uniform appearance. The corresponding SEM images further reveal that BG possesses a loose and uneven macroporous network while BCG and MBCG exhibit denser and more uniform microstructures. It is indicated that the incorporation of biochar plays a key role in stabilizing the structure inside the gels as it can effectively stabilize the bubbles produced in the foaming process. In addition, EDX analysis (Fig. S3) also confirms the occurrence of elemental Mn on

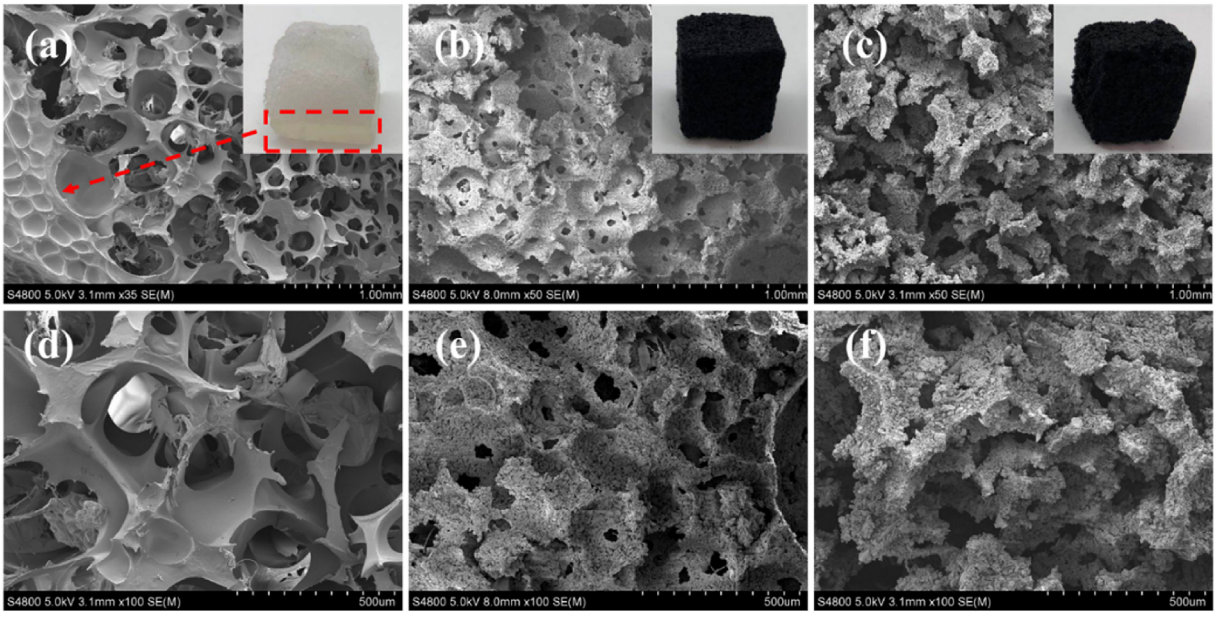

Fig. 3. SEM images of BG (a, d), BCG (b, e) and MBCG (c, f) at different magnifications. (The inset is the corresponding digital photographs).

MBCG as its spectrum showed a new peak for Mn.

In order to gain insight into the porous structures of the samples, the N_2 adsorption-desorption test was carried out with the isotherms and BJH pore size distribution curves shown in Fig. 4. The BET specific surface areas (SSA) and porous structure parameters are summarized in Table S1. Based on the IUPAC classification, the isotherms of both BG and BCG conform to type III, representing a typical macroporous structure, with SSA only of 0.31 and 1.62 $m^2 g^{-1}$, respectively. In contrast, the pristine BC exhibits combined characteristics of type II and IV isotherms with H_3 hysteresis loop representing the occurrence of well-connected mesostructured phases (Li et al., 2019). The inferior pore structure of BCG compared to BC indicates that some micropores and mesopores in BC particles may be blocked after the polymerization process. However, it is worthwhile to note that the MBCG exhibits a similar isotherm shape to MBC with SSA up to 31.17 $m^2 g^{-1}$, demonstrating that the hierarchical porous structure of MBC could be well retained when crosslinked with PAM. This discrepancy could probably be due to the different pore size distribution and pore width of BC and MBC. As shown in Fig. 4b and Table S1, there are a large number of micropores in BC with pore width of 2.74 nm, while more mesopores and macropores could be observed in MBC with pore width increased to 3.61 nm. The increased pore width of MBC could be attributed to the oxidation of $KMnO_4$ which might cause the destruction of some micropore structures and transform some micropores into meso- or macropores. Generally, micropores were easily blocked, while the mesopores and macropores could be efficiently kept, thus endowing MBCG with much better pore structure. In addition, as for the BC, the BET surface area of BC decreased after modification, which may be ascribed to the partial pore blockages caused by the MnO_2 particles formed on the biochar surface. Similar phenomena were also observed in other literature related to MnO_2 loaded biochars (Song et al., 2014; Liang et al., 2017). In summary, the well-developed mesoporous structure, relatively high surface area and large pore width of MBCG are probably superior for the diffusion of pollutants into the inner pore system of the sorbents and the subsequent adsorption removal (Deng et al., 2017).

TG and DTG analysis were further performed to evaluate the thermal stabilities of the fabricated biochars and gels. The

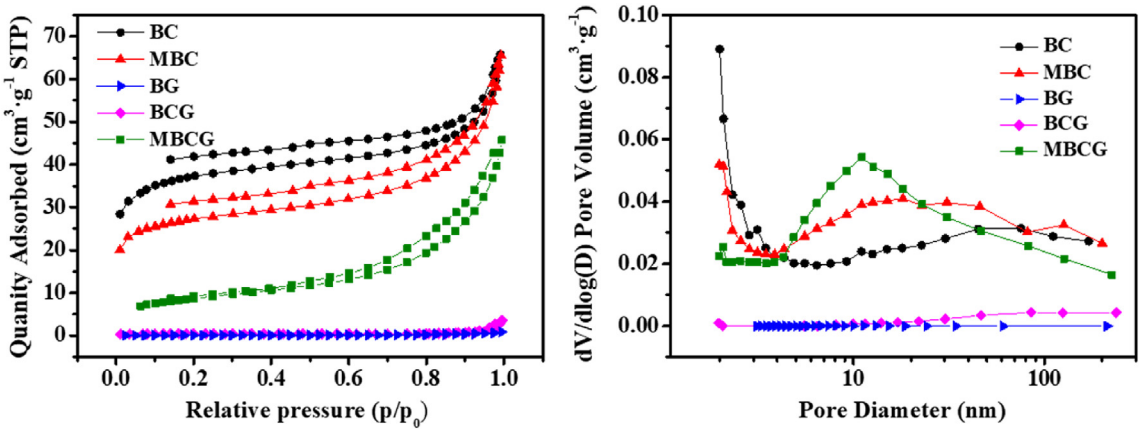

Fig. 4. N_2 adsorption-desorption analysis curves of BC, MBC, BG, BCG, and MBCG: (a) isotherms (b) BJH pore size distributions.

thermogravimetric analyses (TGA) and the differential thermogravimetric data (DTG) curves of the samples are shown in Fig. S4. As for the gels, a sharp decrease in weight was observed between 250 °C and 375 °C of BG, which is due to the depolymerization of polyacrylamide network (Kaşgöz et al., 2003; Yang et al., 2009; Ma et al., 2018). Interestingly, BCG and MBCG show a similar pattern of gradual weight loss in the whole process and their thermostability significantly increased compared to BG, even comparable to those of BC and MBC. The above results manifested that the thermostability of PAMG could be pronouncedly improved by encapsulating biochars and the obtained gels exhibit excellent thermostability for practical applications. Additionally, the final weight residues of BC, MBC, BG, BCG, and MBCG were 79.8%, 75.6%, 15.0%. 70.9%, and 62.0%, respectively, which revealed that the actual biochar loading ratios in BCG and MBCG were 70.0% and 62.2%, respectively.

Considering the separation and regeneration of the gels in practical application, the mechanical properties and structural stabilities were further tested. The supplementary video indicates that the MBCG shows high structural flexibility and elasticity under mechanic compression, and it could be compressed to a large degree without breaking apart. Upon freeing the applied force, it can be instantly recovered to its original form. The mechanical strength of compressive stress-strain curves for the gels are shown in Fig. 5. At a set strain of about 50%, two distinct regions appear in the curves. The initial linear elastic region ($\varepsilon < 35\%–40\%$) at relatively low-stress levels after the second cycle, indicating a typical feature of porous material with high porosity and softness (Chen et al., 2019). The curves become compact and steep at $\varepsilon > 35\%–40\%$ with the rapidly increased stress, which is mainly attributed to the densification of gels. The maximum Young's modulus at 50% strain of BCG and MBCG was found to be 28.9 kPa and 18.7 kPa, which was significantly higher than that of BG (4.3 kPa). In addition, the irrecoverable plastic deformation of BCG (2%) and MBCG (6%) were much lower compared that of BG (12%). The enhanced mechanical properties after incorporating biochars into the PAMG network could be attributed to the following reasons. Firstly, the biochar particles (BC or MBC) can act as reinforcing nanofillers for enhancing the mechanical performance of the hydrogel (Fan et al., 2013). In general, the addition of inorganic ultrafine particles can improve the regularity of the polymer hydrogel network structure, the degree of freedom of the crosslinked structure, and the flexibility of the polymer chain, thus playing a vital role in enhancing the mechanical performance (Chu et al., 2019; Sakai et al., 2008). Secondly, it is well known that the homogenous dispersion of particles in hydrogel is the key to achieving the reinforcement effect (Yue et al., 2019). In this study, the ball-milled biochars were well dispersed in the PAMG matrix without obvious aggregation, which could help transfer the compressive stress from polymer chains to biochar. Thirdly, the introduced biochar could serve as new chemical crosslinking points in the structure of hydrogel through intermolecular hydrogen bonding or covalent bonding with the PAM chains as evidenced by the FTIR analysis, thus further enhanced the mechanical strength of BCG and MBCG. Overall, the mechanical performance of the MBCG renders it suitable for separating and reusing in practical applications.

Supplementary video related to this article can be found at https://doi.org/10.1016/j.chemosphere.2019.124745

3.2. Sorption kinetic and isotherms

Based on the successful construction of 3D MnO_2-modified biochar porous hydrogel, sorption kinetics of Cd(II) and Pb(II) onto MBCG were firstly employed to evaluate its potential ability for heavy metals removal, together with BC, MBC, BCG as comparisons. As shown in Fig. 6a–d, the equilibrium time for the adsorption of Cd(II) and Pb(II) needed for both BCG and MBCG are similar to that of BC and MBC, indicative of an enhanced kinetic performance for the porous gels compared to that of the traditional compact bulk material which has poor sorption kinetics. The rapid adsorptions could be ascribed to the 3D loose and porous structures and their excellent water penetration created by the foaming process, which can provide metal ions with easier access to the adsorption sites. Additionally, the much higher adsorption capacity but slightly slower adsorption rate for the samples after modification might be resulted by the enhanced diffusion with larger pore width and pore volume (Wan et al., 2016). The pseudo-first-order model and pseudo-second-order model were employed to fit kinetic data for further analysis and their corresponding equations are shown in the Supplementary Material. Fitting curves of these models are also plotted in Fig. 6a–d while the corresponding parameter values and correlation coefficients for each system are calculated and listed in Table S2. Similar to the results of previous studies, the adsorption of Cd(II) and Pb(II) exhibited an initial rapid period, followed by a relatively short decreasing step before reaching stability (Wang et al., 2015a). The initial quick rate of adsorption could be attributed to adequate unoccupied adsorptive sites as well as driving force of great concentration gradients. With free active sites become gradually occupied and enhanced repulsive force on the solid-liquid interface, the adsorption rate decreased and then reached to equilibrium (Zhang et al., 2018). Compared with pseudo-first-order kinetics, the pseudo-second-order kinetic model is more suitable to describe the Cd(II) and Pb(II) adsorption kinetic behavior by the samples with a consistently higher regression coefficient and a good agreement between theoretical and experimental Q_e values, implying that chemical adsorption involving covalent forces through sharing or exchange of electrons between the adsorbent and adsorbate could be the rate-controlling mechanism for the adsorption of Cd(II) and Pb(II) on the samples (Liu et al., 2016).

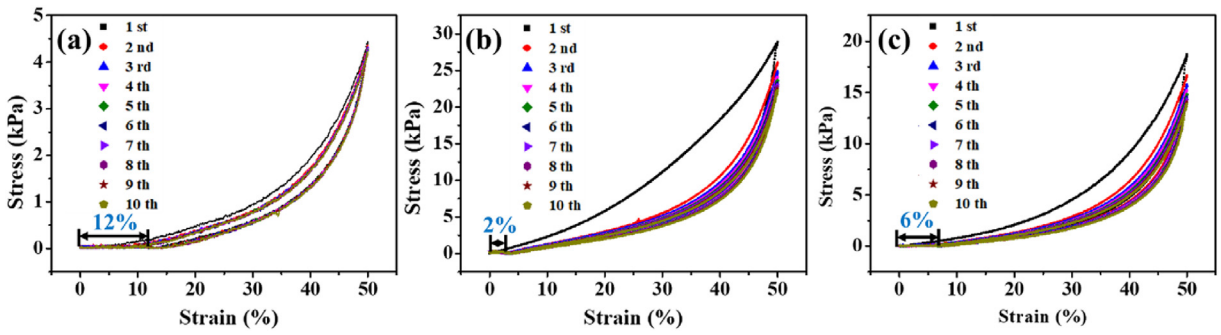

Fig. 5. Compressive stress-strain curves of BG (a), BCG (b) and MBCG (c) compressed to 50% strain.

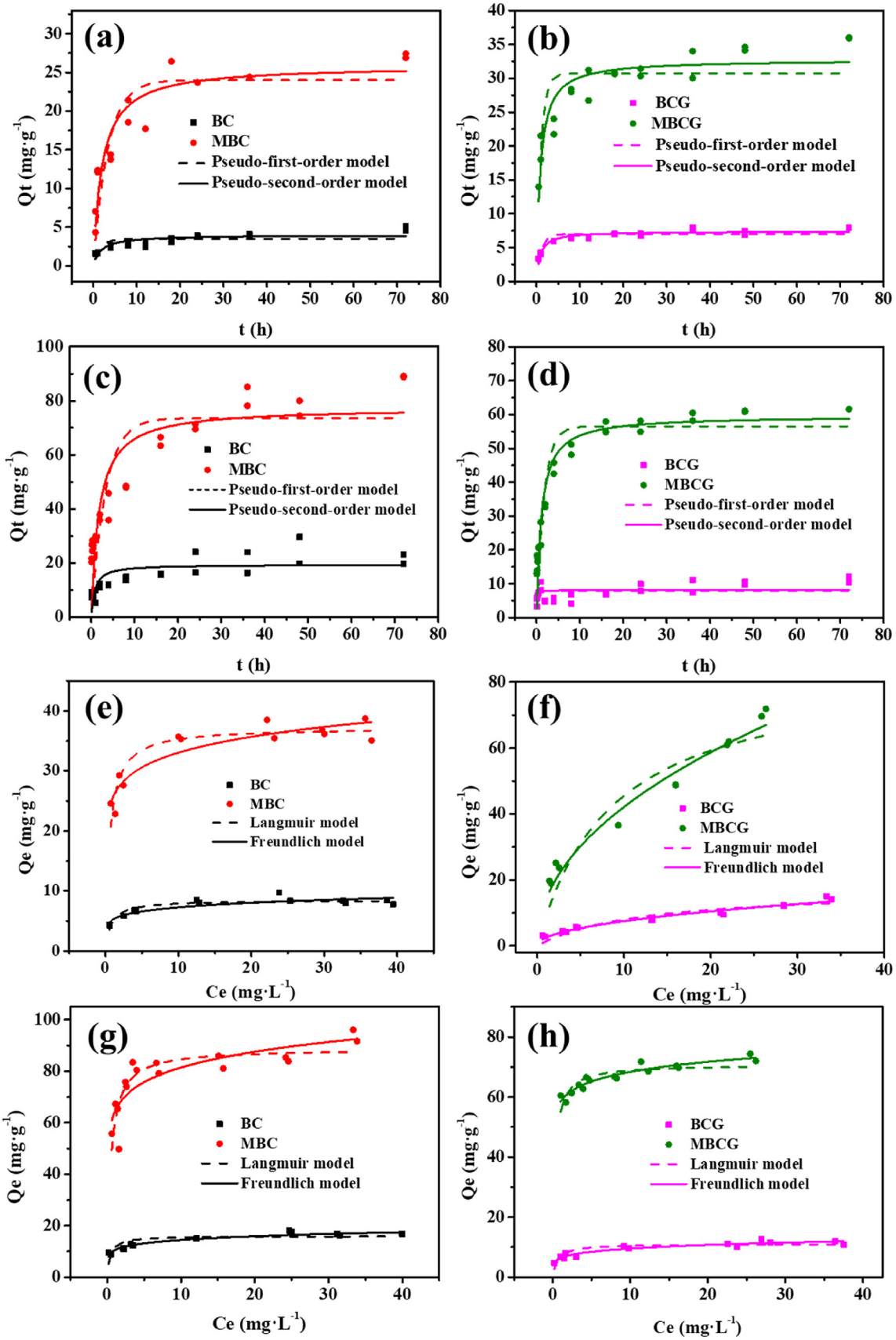

Fig. 6. Adsorption kinetics of Cd(II) and Pb(II) by BC, MBC, BG, BCG and MBCG, and the corresponding kinetic fitting curves: (a, b) Cd(II) and (c, d) Pb(II); adsorption isotherms of Cd(II) and Pb(II) by BC, MBC, BG, BCG and MBCG and the corresponding isotherm fitting curves: (e, f) Cd(II) and (g, h) Pb(II).

In order to further examine the Cd(II) and Pb(II) adsorption capacities, the adsorption isotherm studies were performed on BC, MBC, BCG, and MBCG under equilibrium conditions, the commonly used two-parameter Langmuir and Freundlich models were simulated and the equations are shown in the Supplementary Material. The fitting curves were depicted in Fig. 6e–h and the corresponding fitting parameters are summarized in Table S3.

As shown, the calculated values of correlation coefficient (R^2) suggested that the Freundlich model well fit the data for Cd(II) and Pb(II) adsorption onto all the samples, indicative of multi-site adsorption on heterogeneous adsorbate surfaces. The K_F parameter is different for each test and all the n^{-1} values are lower than 1, which suggested the adsorption process on these samples are favorable and the sorption processes might have taken place through electrostatic interaction, ion-exchange or a combined mechanism (Paulino et al., 2007; Afzal et al., 2018). The Q_m based on the Langmuir model of Cd(II) onto BC, MBC, BCG, and MBCG was 8.84, 37.23, 17.41, and 84.76 mg g^{-1}, respectively, while the maximum adsorption amount of Pb(II) onto BC, MBC, BCG, and MBCG was 16.02, 88.84, 11.07, and 70.90 mg g^{-1}, respectively. In fact, considering the biochar percentages in BCG (70.0%) and MBCG (62.2%) determined by TGA analysis and the negligible adsorption capacities for BG on Cd(II) and Pb(II) evidenced by the pre-experiments (data not shown), it can be calculated that the adsorption capacity of BC component in BCG on Cd(II) and Pb(II) is 24.9 and 15.8 mg g^{-1}, respectively, while the adsorption capacity of MBC component in MBCG on Cd(II) and Pb(II) is 136.3 and 114.0 mg g^{-1}, respectively. The specific surface area is one of the most important parameters for absorbents in practical application. According to the literature, the adsorption capacity increases with the increase of the specific surface area of the adsorbents (Zhang et al., 2019a). However, the uptaking capacities of MBC on Cd(II) and Pb(II) were 3.4 and 4.5 times higher than those of BC, demonstrating significantly enhanced removal capacities of MBC despite its lower BET surface area. This discrepancy may be explained by the deposition of synthesized MnO_2 on the surface of MBC, which enhanced the extra adsorption sites for the attachment of Cd(II) and Pb(II). Moreover, the adsorption capacities of MBCG on Cd(II) and Pb(II) were 4.5 and 6.2 times higher than those of BCG. It is indicated that the adsorption capacity ratio of MBCG to BCG was higher than that of MBC to BC, which can be attributed not only to the load of MnO_2 on MBCG but also its larger surface area.

Generally, transforming powder adsorbents into bulk adsorbents would increase the resistance of pollutant diffusion inside the adsorbent, thus causing the adsorption efficiency of bulk adsorbent remarkably lower than its parent powder materials (Zhao et al., 2019). However, the BCG and MBCG exhibit comparable or even higher adsorption performance than their corresponding powder biochars, which is at odds with most previous studies. Taken together, the significantly enhanced removal capacities of MBCG can be explained by the following synergistic effects. Firstly, the introduced MnO_2 particles could serve as new active adsorption sites with the increased negatively charged oxygen-containing functional groups (such as hydroxyl, carboxyl and carbonyl groups) which could provide more opportunities for the adsorption of heavy metal ions through electrostatic attraction as well as the ion exchange between the proton and the metal ions (Li et al., 2017). Secondly, the 3D PAMG network could effectively prevent the agglomeration of biochar particles, thus making the active adsorption sites fully exposed. Thirdly, the unique porous interconnected structure can effectively trap heavy metal ions, resulting in the in-depth extension from the surface adsorption to bulk uptake.

To further evaluate the adsorption performance of MBCG, we compare it with some other biochars or polyacrylamide gels related adsorbents for Cd(II) and Pb(II) removal described in the literature. Generally, higher initial concentration and pH value could result in higher heavy metal adsorption capacity. Thus, as shown in Tables S4 and S5, the maximum sorption capacities of MBCG are comparable or even higher than those of many other adsorbents reported at similar equilibrium concentrations. Moreover, the supplementary material also reveals the raw material cost of MBCG is very cost-effective.

3.3. Desorption and regeneration experiments

Five adsorption-desorption cycles were conducted to investigate the regeneration and reusability of the gels (Fig. 7). As shown, under the experiment condition the adsorption capacities of the virgin BCG and MBCG on Cd(II) was 2.65 and 16.88 mg g^{-1}, respectively, while those of the virgin BCG and MBCG on Pb(II) was 9.32 and 42.48 mg g^{-1}, respectively. After five recycles, the adsorption capacities of MBCG were 15.55 mg g^{-1} on Cd(II) and 34.21 mg g^{-1} on Pb(II), still retaining 92.1% and 80.5% of the initial adsorption capacities of virgin MBCG. However, the adsorption capacities of BCG decreased to only 0.22 mg g^{-1} and 2.53 mg g^{-1} at the last cycle, indicating huge losses (78.4% and 72.9%) in comparison to those of the fresh BCG. The much better regeneration performance for MBCG can be attributed to its mesoporous structure which can effectively prevent the loss of inner active sites

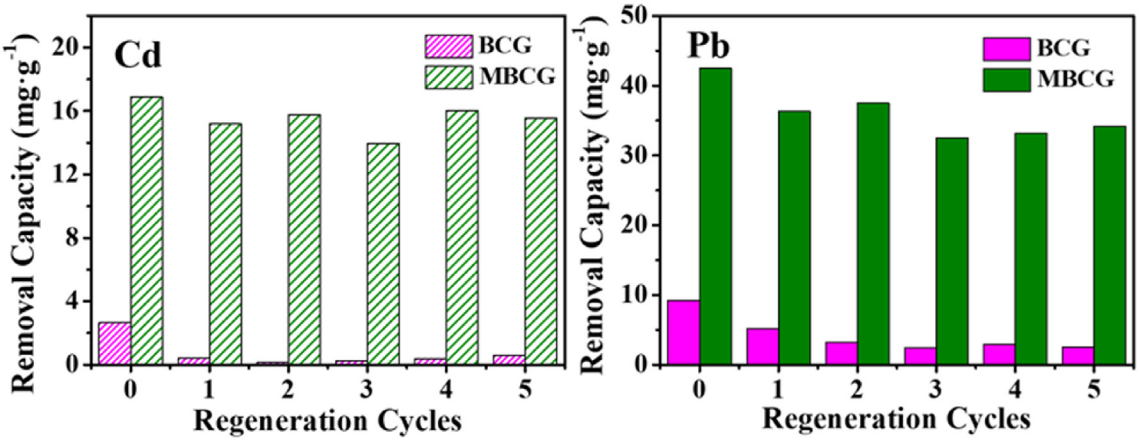

Fig. 7. Regeneration and recycle performance of the BCG and MBCG on Cd(II) and Pb(II).

during the cycles. The regenerated MBCG after the initial HNO_3 and subsequent NaOH treatment still maintain its original shape and can be repeatedly used for more than five cycles. To further prove its stability after desorption, the SEM analysis of the desorbed MBCG was performed. The results (Fig. S6) show that the morphologies of the regenerated MBCG was nearly unchanged, indicating its excellent structural and chemical stability. Accordingly, the enhanced and reversible adsorptive performance together with excellent stability makes the fabricated MBCG a perfect candidate for heavy metal ion remediation. MBCG can be rapidly separated and easily regenerated with an excellent reusability, which could retain 92.1% and 80.5% of the initial adsorption capacities of Cd(II) and Pb(II) after five cycles.

4. Conclusion

In this study, a 3D MBCG composite adsorbent with well-interconnected channels for removing Cd(II) and Pb(II) from polluted water is successfully synthesized. MnO_2 modified biochars were successfully introduced and homogeneously distributed in 3D hydrogels. The MnO_2 modified biochar effectively stabilized the bubbles during the foaming process and endowed the composite hydrogels with more uniform pores, enhanced thermostability and reinforced mechanic strength. Findings from batch sorption experiments indicated that the well distributed particles and 3D porous morphology of the gel were in favor of the exposure of more adsorption active sites thus equipped the gel with superior adsorption performance (high adsorption capacities and rapid diffusion). In addition, considering its simple production process, low-cost raw materials, ease of separation operation as well as desirable reusability, it is expected that MBCG will have potentially wide application in Cd(II) and Pb(II) removal from aquatic and soil systems.

Acknowledgments

This work was financially supported by the National Natural Science Foundation of China (51778598), the China-Japanese Research Cooperative Program (2016YFE0118000) and the Science and Technology Program of Xiamen (3502Z20172022).

Appendix A. Supplementary data

Supplementary data to this article can be found online at https://doi.org/10.1016/j.chemosphere.2019.124745.

References

Afzal, M.Z., Sun, X., Liu, J., Song, C., Wang, S., Javed, A., 2018. Enhancement of ciprofloxacin sorption on chitosan/biochar hydrogel beads. Sci. Total Environ. 639, 560–569.
Ahmed, M.B., Zhou, J.L., Ngo, H.H., Guo, W., Chen, M., 2016. Progress in the preparation and application of modified biochar for improved contaminant removal from water and wastewater. Bioresour. Technol. 214, 836–851.
Burtch, N.C., Jasuja, H., Walton, K.S., 2014. Water stability and adsorption in metal-organic frameworks. Chem. Rev. 114, 10575–10612.
Chen, Z., Chen, B., Chiou, C.T., 2012. Fast and slow rates of naphthalene sorption to biochars produced at different temperatures. Environ. Sci. Technol. 46, 11104–11111.
Chen, X., Lai, D., Yuan, B., Fu, M., 2019. Tuning oxygen clusters on graphene oxide to synthesize graphene aerogels with crumpled nanosheets for effective removal of organic pollutants. Carbon 143, 897–907.
Chipasa, K.B., 2003. Accumulation and fate of selected heavy metals in a biological wastewater treatment system. Waste Mange 23, 135–143.
Chu, Y.Y., Song, X.F., Zhao, H.X., 2019. Water-swellable, tough, and stretchable inorganic-organic sulfoaluminate cement/polyacrylamide double-network hydrogel composites. J. Appl. Polym. Sci. 136, 47905.
Demirbas, A., 2004. Adsorption of lead and cadmium ions in aqueous solutions onto modified lignin from alkali glycerol delignication. J. Hazard Mater. 109, 221–226.
Deng, J., Liu, Y., Liu, S., Zeng, G., Tan, X., Huang, B., Tang, X., Wang, S., Hua, Q., Yan, Z., 2017. Competitive adsorption of Pb(II), Cd(II) and Cu(II) onto chitosan-pyromellitic dianhydride modified biochar. J. Colloid Interface Sci. 506, 355–364.
Dong, C., Lu, J., Qiu, B., Shen, B., Xing, M., Zhang, J., 2018. Developing stretchable and graphene-oxide-based hydrogel for the removal of organic pollutants and metal ions. Appl. Catal. B Environ. 222, 146–156.
Fan, J., Shi, Z., Lian, M., Li, H., Yin, J., 2013. Mechanically strong graphene oxide/sodium alginate/polyacrylamide nanocomposite hydrogel with improved dye adsorption capacity. J. Mater. Chem. 1, 7433.
Fu, F., Wang, Q., 2011. Removal of heavy metal ions from wastewaters: a review. J. Environ. Manag. 92, 407–418.
Getachew, B.A., Kim, S., Kim, J., 2016. Self-healing hydrogel pore-filled water filtration membranes. Environ. Sci. Technol. 51, 905–913.
Godiya, C.B., Cheng, X., Li, D., Chen, Z., Lu, X., 2019. Carboxymethyl cellulose/polyacrylamide composite hydrogel for cascaded treatment/reuse of heavy metal ions in wastewater. J. Hazard Mater. 364, 28–38.
Kaşgöz, H., Özgümüş, S., Orbay, M., 2003. Modified polyacrylamide hydrogels and their application in removal of heavy metal ions. Polymer 44, 1785–1793.
Lai, C., Zhang, M., Li, B., Huang, D., Zeng, G., Qin, L., Liu, X., Yi, H., Cheng, M., Li, L., Chen, Z., Chen, L., 2019. Fabrication of CuS/BiVO4 (0 4 0) binary heterojunction photocatalysts with enhanced photocatalytic activity for Ciprofloxacin degradation and mechanism insight. Chem. Eng. J. 358, 891–902.
Li, H., Dong, X., Da Silva, E.B., de Oliveira, L.M., Chen, Y., Ma, L.Q., 2017. Mechanisms of metal sorption by biochars: biochar characteristics and modifications. Chemosphere 178, 466–478.
Li, B., Lai, C., Xu, P., Zeng, G., Huang, D., Qin, L., Yi, H., Cheng, M., Wang, L., Huang, F., Liu, S., Zhang, M., 2019. Facile synthesis of bismuth oxyhalogen-based Z-scheme photocatalyst for visible-light-driven pollutant removal: kinetics, degradation pathways and mechanism. J. Clean. Prod. 225, 898–912.
Liang, J., Li, X., Yu, Z., Zeng, G., Luo, Y., Jiang, L., Yang, Z., Qian, Y., Wu, H., 2017. Amorphous MnO_2 modified biochar derived from aerobically composted swine manure for adsorption of Pb(II) and Cd(II). Acs Sustain Chem Eng 5, 5049–5058.
Liu, J., Ge, X., Ye, X., Wang, G., Zhang, H., Zhou, H., Zhang, Y., Zhao, H., 2016. 3D graphene/δ-MnO_2 aerogels for highly efficient and reversible removal of heavy metal ions. J. Mater. Chem. 4, 1970–1979.
Lo, S., Wang, S., Tsai, M., Lin, L., 2012. Adsorption capacity and removal efficiency of heavy metal ions by Moso and Ma bamboo activated carbons. Chem. Eng. Res. Des. 90, 1397–1406.
Ma, J., Liu, Y., Ali, O., Wei, Y., Zhang, S., Zhang, Y., Cai, T., Liu, C., Luo, S., 2018. Fast adsorption of heavy metal ions by waste cotton fabrics based double network hydrogel and influencing factors insight. J. Hazard Mater. 344, 1034–1042.
Matlock, M.M., Howerton, B.S., Atwood, D.A., 2002. Chemical precipitation of heavy metals from acid mine drainage. Water Res. 36, 4757–4764.
Mohan, D., Kumar, H., Sarswat, A., Alexandre-Franco, M., Pittman, C.U., 2014. Cadmium and lead remediation using magnetic oak wood and oak bark fast pyrolysis bio-chars. Chem. Eng. J. 236, 513–528.
Morgan, J.J., Stumm, W., 1964. Colloid-chemical properties of manganese dioxide. J. Colloid Sci. 19, 347.
Oliveira, F.R., Patel, A.K., Jaisi, D.P., Adhikari, S., Lu, H., Khanal, S.K., 2017. Environmental application of biochar: current status and perspectives. Bioresour. Technol. 246, 110–122.
Paulino, A., Guilherme, M., Reis, A., Tambourgi, E., Nozaki, J., Muniz, E., 2007. Capacity of adsorption of Pb^{2+} and Ni^{2+} from aqueous solutions by chitosan produced from silkworm chrysalides in different degrees of deacetylation. J. Hazard Mater. 147, 139–147.
Rajapaksha, A.U., Chen, S.S., Tsang, D.C.W., Zhang, M., Vithanage, M., Mandal, S., Gao, B., Bolan, N.S., Ok, Y.S., 2016. Engineered/designer biochar for contaminant removal/immobilization from soil and water: potential and implication of biochar modification. Chemosphere 148, 276–291.
Sakai, T., Matsunaga, T., Yamamoto, Y., Ito, C., Yoshida, R., Suzuki, S., Sasaki, N., Shibayama, M., Chung, U., 2008. Design and fabrication of a high-strength hydrogel with ideally homogeneous network structure from tetrahedron-like macromonomers. Macromolecules 41, 5379–5384.
Song, Z., Lian, F., Yu, Z., Zhu, L., Xing, B., Qiu, W., 2014. Synthesis and characterization of a novel MnOx-loaded biochar and its adsorption properties for Cu^{2+} in aqueous solution. Chem. Eng. J. 242, 36–42.
Vaca Mier, M., López Callejas, R., Gehr, R., Jiménez Cisneros, B.E., Alvarez, P.J.J., 2001. Heavy metal removal with Mexican clinoptilolite: multi-component ionic exchange. Water Res. 35, 373–378.
Wan, S., He, F., Wu, J., Wan, W., Gu, Y., Gao, B., 2016. Rapid and highly selective removal of lead from water using graphene oxide-hydrated manganese oxide nanocomposites. J. Hazard Mater. 314, 32–40.
Wang, J., Chen, C., 2014. Chitosan-based biosorbents: modification and application for biosorption of heavy metals and radionuclides. Bioresour. Technol. 160, 129–141.
Wang, H., Gao, B., Wang, S., Fang, J., Xue, Y., Yang, K., 2015a. Removal of Pb(II), Cu(II), and Cd(II) from aqueous solutions by biochar derived from $KMnO_4$ treated hickory wood. Bioresour. Technol. 197, 356–362.
Wang, M.C., Sheng, G.D., Qiu, Y.P., 2015b. A novel manganese-oxide/biochar composite for efficient removal of lead(II) from aqueous solutions. Int J Environ Sci Te 12, 1719–1726.
Wang, X., Huang, K., Chen, Y., Liu, J., Chen, S., Cao, J., Mei, S., Zhou, Y., Jing, T., 2018. Preparation of dumbbell manganese dioxide/gelatin composites and their application in the removal of lead and cadmium ions. J. Hazard Mater. 350,

46–54.
Wingenfelder, U., Nowack, B., Furrer, G., Schulin, R., 2005. Adsorption of Pb and Cd by amine-modified zeolite. Water Res. 39, 3287–3297.
Xiao, X., Chen, B., Chen, Z., Zhu, L., Schnoor, J.L., 2018. Insight into multiple and multilevel structures of biochars and their potential environmental applications: a critical review. Environ. Sci. Technol. 52, 5027–5047.
Xing, S., Hu, C., Qu, J., He, H., Yang, M., 2008. Characterization and reactivity of MnO_x supported on mesoporous zirconia for herbicide 2,4-D mineralization with ozone. Environ. Sci. Technol. 42, 3363–3368.
Yang, F., Li, G., He, Y., Ren, F., Wang, G., 2009. Synthesis, characterization, and applied properties of carboxymethyl cellulose and polyacrylamide graft copolymer. Carbohydr. Polym. 78, 95–99.
Yang, F., Zhang, S., Li, H., Li, S., Cheng, K., Li, J., Tsang, D.C.W., 2018. Corn straw-derived biochar impregnated with α-FeOOH nanorods for highly effective copper removal. Chem. Eng. J. 348, 191–201.
Yue, Y., Wang, X., Han, J., Yu, L., Chen, J., Wu, Q., Jiang, J., 2019. Effects of nanocellulose on sodium alginate/polyacrylamide hydrogel: mechanical properties and adsorption-desorption capacities. Carbohydr. Polym. 206, 289–301.
Zhang, M., Gao, B., Varnoosfaderani, S., Hebard, A., Yao, Y., Inyang, M., 2013a. Preparation and characterization of a novel magnetic biochar for arsenic removal. Bioresour. Technol. 130, 457–462.
Zhang, Q., Du, Q., Hua, M., Jiao, T., Gao, F., Pan, B., 2013b. Sorption enhancement of lead ions from water by surface charged polystyrene-supported nano-zirconium oxide composites. Environ. Sci. Technol. 47, 6536–6544.
Zhang, W., Deng, Q., He, Q., Song, J., Zhang, S., Wang, H., Zhou, J., Zhang, H., 2018. A facile synthesis of core-shell/bead-like poly (vinyl alcohol)/alginate@PAM with good adsorption capacity, high adaptability and stability towards Cu(II) removal. Chem. Eng. J. 351, 462–472.
Zhang, D., Wang, L., Zeng, H., Yan, P., Nie, J., Sharma, V.K., Wang, C., 2019a. A three-dimensional macroporous network structured chitosan/cellulose biocomposite sponge for rapid and selective removal of mercury(II) ions from aqueous solution. Chem. Eng. J. 363, 192–202.
Zhang, M., Lai, C., Li, B., Huang, D., Zeng, G., Xu, P., Qin, L., Liu, S., Liu, X., Yi, H., Li, M., Chu, C., Chen, Z., 2019b. Rational design 2D/2D BiOBr/CDs/g-C3N4 Z-scheme heterojunction photocatalyst with carbon dots as solid-state electron mediators for enhanced visible and NIR photocatalytic activity: kinetics, intermediates, and mechanism insight. J. Catal. 369, 469–481.
Zhao, D., Tian, Y., Jing, X., Lu, Y., Zhu, G., 2019. PAF-1@cellulose nanofibril composite aerogel for highly-efficient removal of bisphenol A. J. Mater. Chem. 7, 157–164.
Zhu, W., Zhang, Y., Wang, P., Yang, Z., Yasin, A., Zhang, L., 2019. Preparation and applications of salt-resistant superabsorbent poly (acrylic acid-acrylamide/fly ash) composite. Materials 12, 596.